

Near infrared spectroscopy of M dwarfs. IV. A preliminary survey on the carbon isotopic ratio in M dwarfs *

Takashi TSUJI

*Institute of Astronomy, School of Science, The University of Tokyo, 2-21-1 Osawa, Mitaka-shi, Tokyo, 181-0015
ttsuji@ioa.s.u-tokyo.ac.jp*

(Received ; accepted)

Abstract

Carbon isotopic ratios are estimated in 48 M dwarfs based on the medium resolution near infrared spectra ($\lambda/\Delta\lambda \approx 20000$) of ^{13}CO (3,1) band. We find clear evidence for the presence of a ^{13}CO feature for the first time in the spectra of M dwarfs. Spectral resolution of our observed data, however, is not high enough to analyze the ^{13}CO feature directly. Instead, we compare observed spectrum with synthetic spectra assuming $^{12}\text{C}/^{13}\text{C} = 10, 25, 50, 100,$ and 200 for each of 48 M dwarfs and estimate the best possible $^{12}\text{C}/^{13}\text{C}$ ratio by the chi-square analysis. The resulting $^{12}\text{C}/^{13}\text{C}$ ratios in M dwarfs distribute from 39 to a lower limit of 200. The mean value of 31 M dwarfs for which $^{12}\text{C}/^{13}\text{C}$ ratios are determined (i.e., excluding those with the lower limit only) is $(^{12}\text{C}/^{13}\text{C})_{\text{dM}} = 87 \pm 21$ (p.e.), and that of 48 M dwarfs including those with the lower limit of 200 is $(^{12}\text{C}/^{13}\text{C})_{\text{dM}} > 127 \pm 41$ (p.e.). These results are somewhat larger than the $^{12}\text{C}/^{13}\text{C}$ ratio of the present interstellar matter (ISM) determined from the molecular lines observed in the millimeter and optical wavelength regions. Since the amount of ^{13}C in the ISM has increased with time due to mass-loss from evolved stars, the $^{12}\text{C}/^{13}\text{C}$ ratios in M dwarfs, reflecting those of the past ISM, should be larger than those of the present ISM. In M dwarfs, $\log^{13}\text{C}/^{12}\text{C}$ plotted against $\log A_{\text{C}}$ shows a large scatter without clear dependence on the metallicity. This result shows a marked contrast to $\log^{16}\text{O}/^{12}\text{C}$ ($= \log A_{\text{O}}/A_{\text{C}}$) plotted against $\log A_{\text{C}}$, which shows a rather tight correlation with a larger value at the lower metallicity. Such a contrast can be a natural consequence that ^{16}O and ^{12}C are the primary products in the stellar nuclear synthesis while ^{13}C is the secondary product, at least partly.

Key words: ISM: abundances – Stars: abundances – Stars: atmospheres – Stars: late-type – Stars: low mass

1. Introduction

Besides the elemental abundances, isotopic ratios in stars and interstellar matter (ISM) provide important clues on stellar evolution and Galactic chemical evolution. However, isotopic effects are prominent only in molecular spectra but not in atomic spectra. For this reason, isotopic analysis has mostly been done on molecular spectra observed in cool celestial objects such as cool stars and the ISM. Because of this limitation, our knowledge on the isotopic abundances in the Universe has been rather poor compared to that on the elemental abundances. On the other hand, spectroscopic analyses of the isotopic ratios are somewhat simpler, compared to those of the elemental abundances, in that the isotopic ratios are relatively insensitive to the physical condition of the environments where spectral lines are formed. For this reason, isotopic analyses have extensively been done on the spectra of cool stars since the middle of the 20-th century even when analyses on the elemental abundances were more difficult.

For example, initial attempt to determine the $^{12}\text{C}/^{13}\text{C}$ ratio in cool giant stars has been done by Greene (1969), who showed that the $^{12}\text{C}/^{13}\text{C}$ ratio in red giant stars

is decreased compared to the solar system value of 89.9 (Anders & Grevesse 1989). Then, extensive analyses on the $^{12}\text{C}/^{13}\text{C}$ ratio in G and K giant stars have been done with the use of photoelectric scans of the CN red system (Day et al. 1973; Tomkin & Lambert 1974; Tomkin et al. 1975; Dearborn et al. 1975). The results confirmed that the products of the CNO cycle are dredged-up in the red giant phase, but the resulting $^{12}\text{C}/^{13}\text{C}$ ratios appeared to be too small compared with the theoretical predictions (e.g., Dearborn et al. 1976). Studies on the $^{12}\text{C}/^{13}\text{C}$ ratio were extended to red supergiants (Lambert et al. 1974) and to AGB stars with the use of the high resolution FTS spectra (Smith & Lambert 1986, 1990; Tsuji 2008). The results on oxygen-rich giants, supergiants, and AGB stars revealed that these stars contribute to lower the $^{12}\text{C}/^{13}\text{C}$ ratio in the ISM by their mass-loss.

Historically, it was on carbon stars that studies on carbon isotopes in stellar spectra have initiated: It was nearly a century ago when ^{13}C bearing molecules were identified by the C_2 Swan bands, first as $^{12}\text{C}^{13}\text{C}$ (Sanford 1929) and next as $^{13}\text{C}^{13}\text{C}$ (Menzel 1930) in carbon stars (also referred to as R and N type stars). Initial works suggested that the $^{12}\text{C}/^{13}\text{C}$ ratios in most carbon stars are in the range of 2 – 20, except for a few exceptional case (McKellar 1960 and references cited therein). This result suggested that the $^{12}\text{C}/^{13}\text{C}$ ratios in carbon stars may be

* Based on data collected at Subaru Telescope, which is operated by the National Astronomical Observatory of Japan.

related to the equilibrium value of the $^{12}\text{C}/^{13}\text{C}$ ratio in the CN cycle. However, since the $^{12}\text{C}^{12}\text{C}$ Swan bands in carbon stars are very strong and heavily saturated while the $^{12}\text{C}^{13}\text{C}$ Swan bands less saturated, the intensity ratio of $^{12}\text{C}^{12}\text{C}/^{12}\text{C}^{13}\text{C}$ should apparently be small leading to a low $^{12}\text{C}/^{13}\text{C}$ ratio. For this reason, the very low $^{12}\text{C}/^{13}\text{C}$ ratios found in carbon stars can be due to imperfect correction for the saturation effect, and a possibility that $^{12}\text{C}/^{13}\text{C} \approx 100$ was suggested for some cool carbon stars (e.g., Fujita & Tsuji 1977). Since then, many works on the $^{12}\text{C}/^{13}\text{C}$ ratio have been carried out for a large sample of carbon stars: Lambert et al. (1986) determined the $^{12}\text{C}/^{13}\text{C}$ ratios in dozens of N type stars through the analysis of the high resolution FTS spectra of the CN red system, CO first and second overtones, and showed that the $^{12}\text{C}/^{13}\text{C}$ ratios in cool carbon stars extend to as large as the solar system value. Determinations of the $^{12}\text{C}/^{13}\text{C}$ ratios were extended through the analysis of the CN red system to 62 N type stars by Ohnaka & Tsuji (1996) and to 44 carbon stars by Abia & Isern (1997). The results on carbon-rich AGB stars revealed that the $^{12}\text{C}/^{13}\text{C}$ ratios in these stars are generally larger than in oxygen-rich AGB stars and these stars contribute to increase the $^{12}\text{C}/^{13}\text{C}$ ratio in the ISM by their mass-loss.

In contrast, isotopic analyses on cool dwarfs are quite limited, even though extensive analyses on elemental abundances in late-type dwarfs have been done (e.g., Edvardsson et al. 1993). It is true that molecular lines are not so strong in F and G dwarfs. However, the major reasons for this contrast between high and low luminosity stars may be that the high resolution spectroscopy needed to isolate faint isotopic features could be applied more easily to bright high luminous stars on one hand and also some isotopic features appeared to be enhanced in high luminous cool stars due to the evolutionary effects in the stars themselves.

In M dwarfs, determinations of the elemental abundances have also been difficult, but we have shown recently that the carbon and oxygen abundances in M dwarfs could be determined rather accurately by the use of the near infrared spectra of CO and H₂O, respectively (Tsuji & Nakajima 2014, Tsuji et al. 2015, Tsuji & Nakajima 2016, hereafter Papers I, II, and III, respectively). This has been made possible by several reasons: First, the well known difficulty of the continuum in cool stars has been overcome in doing spectroscopic analysis by referring to the pseudo-continuum, which can be evaluated accurately with the use of the recent molecular line-list including many weak lines of H₂O (e.g., Barber et al. 2006; Rothman et al. 2010). Then, spectroscopic analysis can be done essentially the way as referring to the true-continuum, so long as the pseudo-continuum can be defined consistently in the observed and predicted spectra. Second, given that carbon and oxygen abundances are determined from stable molecules such as CO and H₂O, respectively, the problem of photospheric model should not be so serious. This is because CO consumes most of carbon and H₂O most of oxygen left after CO formation, and CO abundance is almost identical with that of C and

H₂O abundance with that of O–C in M dwarfs. For this reason, CO and H₂O abundances are insensitive to the uncertainties of the photospheric structures¹, and carbon and oxygen abundances could be determined rather well despite the use of model photospheres which anyhow cannot be very accurate (as for further details, see e.g., Paper II).

Given that the elemental abundances of at least some elements were well determined in M dwarfs, a further important possibility in M dwarfs is that the isotopic ratios can also be determined from the molecular spectra, at the same time as the elemental abundances in the same object. In the near infrared spectra of M dwarfs, not only $^{12}\text{C}^{16}\text{O}$ but also $^{13}\text{C}^{16}\text{O}$ bands are observed, and the $^{12}\text{C}/^{13}\text{C}$ ratios can be discussed. A problem is that the spectral resolution of our spectra is about $\lambda/\Delta\lambda \approx 20000$ or the velocity resolution is about 16 km s^{-1} . This resolution barely made it possible to measure equivalent widths and hence to determine the elemental abundances of carbon and oxygen (Papers I, II, and III). However, this resolution is not high enough to measure line profiles accurately and hence to analyze faint isotopic features. For this reason, our analysis on the carbon isotopic ratios is necessarily preliminary. Even with this limitation, however, we hope that we can discuss the elemental and isotopic abundances of carbon simultaneously in a large sample of M dwarfs for the first time.

In this paper, we first summarize the known data on our program stars from Papers I, II, and III in section 2. We then investigate how to estimate the $^{12}\text{C}/^{13}\text{C}$ ratios from the spectra of ^{13}CO in section 3. The resulting $^{12}\text{C}/^{13}\text{C}$ ratios, with assessments of the accuracy, are given in section 4. The resulting carbon isotopic ratios in M dwarfs are discussed in comparisons with those of the ISM in section 5.

2. Preparatory data for isotopic analysis

2.1. Observed data

We use the observed data introduced in Paper I (see its Table 1) and III (its Table 1), in which we analyzed $^{12}\text{C}^{16}\text{O}$ and H₂O lines. In this paper, we focus our attention to $^{13}\text{C}^{16}\text{O}$ features recorded on the 24-th order (23437 – 23997 Å) of the echelle spectra observed with the Infrared Camera and Spectrograph (IRCS: Kobayashi et al. 2000) of the Subaru Telescope. The resolution $\lambda/\Delta\lambda$ is about 20000 or the velocity resolution is about 16 km s^{-1} . In our observations, the targets were nodded along the slit, and observations were taken in an ABBA sequence, where A and B stand for the first and second positions on the slit (Paper I). For estimating the signal to noise (S/N) ratio, the noise level is estimated from the difference of the spectra observed at A and B positions. The resulting S/N ratio is given in the last column of Table

¹ It is to be noted that this advantage does not apply to CO in general, but applies to CO in M dwarfs only. In warmer F or G dwarfs, CO abundance is highly sensitive to temperature and cannot be used for accurate abundance analysis (see footnote 9 in Paper I).

3 for each object, and the S/N ratios are mostly between about 50 and 150.

2.2. Stellar data

Our program stars consist of M dwarfs studied so far by us: We first determined the fundamental parameters such as T_{eff} and $\log g$, prepared model photospheres, and determined carbon abundances based on the $^{12}\text{C}^{16}\text{O}$ lines for 42 M dwarfs (Paper I). For 38 objects in these 42 M dwarfs, we also determined oxygen abundances from H_2O lines (Paper II). We then studied additional eight late M dwarfs (Paper III). As a result, we determined carbon and oxygen abundances in $38 + 8 = 46$ M dwarfs.

We did not determine oxygen abundances in four early M dwarfs in which H_2O lines were too weak (Paper II). However, we estimate oxygen abundances in these four M dwarfs with the use of $\log A_{\text{O}}/A_{\text{C}} - \log A_{\text{C}}$ ² relation based on 46 M dwarfs for which carbon and oxygen abundances were determined as noted above. A least square fit to $\log A_{\text{O}}/A_{\text{C}}$ (data reproduced in eighth column of Table 1 and plotted in Fig. 6b) is

$$\log A_{\text{O}}/A_{\text{C}} = 0.270 \log A_{\text{C}} - 0.684, \quad (1)$$

from which we estimate $\log A_{\text{O}}/A_{\text{C}}$ and then $\log A_{\text{O}}$ by the use of the known $\log A_{\text{C}}$. We include these four early M dwarfs with the estimated oxygen abundances in our analysis of the carbon isotopic ratio based on CO spectra in this paper. We think that the use of the estimated oxygen abundance can be acceptable, since CO spectra depend primarily on carbon abundance and effect of oxygen abundance is rather minor.

From the 38 M dwarfs for which C and O abundances were determined, we exclude one object GJ 686 whose spectrum is disturbed by unknown noise. Also, we could not include 2MASS J1835379+325954 in our sample of eight late M dwarfs, since this object is a rapid rotator (Paper III) and isotopic features are completely smeared out. As a result, we have $37 + 7 + 4 = 48$ objects for our analysis of the carbon isotopic ratios in this paper.

For 50 M dwarfs we have analyzed through Papers I to III, object, spectral type, T_{eff} , and $\log g$ are given through first to fourth column in Table 1, and $\log A_{\text{C}}$, $\log A_{\text{O}}$ (including the oxygen abundances estimated with the use of equation 1), and $\log A_{\text{O}}/A_{\text{C}}$ through sixth to eighth column.

table 1: p.16

2.3. Model photospheres

We apply dust-free model photospheres of C series included as a subset of our unified cloudy models (UCMs) for cool dwarfs (Tsuji 2002) throughout this paper. Although we have prepared a grid of model photospheres³,

² We use the notation $A_{\text{El}} = N_{\text{El}}/N_{\text{H}}$, where N_{El} and N_{H} are the number densities of the element El and hydrogen nuclei, respectively.

³ <http://www.mtk.ioa.s.u-tokyo.ac.jp/~ttsuji/export/ucm2>

we generated a specified model for each object based on T_{eff} and $\log g$ given in third and fourth columns of Table 1, respectively (Papers I & III). The chemical composition assumed is based either on the classical solar C and O abundances (Anders & Grevesse 1989; referred to as *case a*; see Table 1 of Tsuji 2002) or on the downward revised ones (Allende Prieto et al. 2002; *case c*), depending on the C and O abundances of each object in columns 6 and 7, respectively, in Table 1. The model we have applied is given in the fifth column of Table 1 for each object, and a model is designated as Ca or Cc/ $T_{\text{eff}}/\log g$. For example, Ca3570c489 implies a model of C series with the *case a* chemical composition, $T_{\text{eff}} = 3570$ K, and $\log g = 4.89$.

2.4. Molecular data

We evaluate line positions of $^{13}\text{C}^{16}\text{O}$ lines based on Dunham coefficients by Guelachivili et al. (1983), and apply the same intensity data as for $^{12}\text{C}^{16}\text{O}$ (Chackerian & Tipping 1983). As for spectroscopic data of H_2O , we continue to apply BT2-HITEMP2010 database (Barber et al. 2006; Rothman et al. 2010) as in Papers I - III.

The BT2-HITEMP2010 line list is largely based on the computed water line list, and its accuracy has been confirmed by extensive testings against astronomical and laboratory data by Barber et al. (2006). We also compare the line list with the observed water lines in sunspot spectra in the spectral region we are to work. For this purpose, we use the Sunspot Umbral Spectrum (Wallace & Livingston 1992) recorded with resolution as high as $R \approx 180000$ ($\text{FWHM} \approx 0.024 \text{ cm}^{-1}$). We find 14 undisturbed water lines between 4200 and 4240 cm^{-1} (or between 23585 and 23810 Å) in the atlas and measured their line positions as given in the second column of Table 2. For comparison, the line positions from the BT2-HITEMP2010 database are given in third column. Since we are using wavelength unit throughout this paper, these values are converted to the wavelength unit (in Å in vacuum) and given in fourth and fifth columns. The difference of the two is given in sixth column for each line. (The upper and lower levels of the transition are given after seventh column.) Although the differences are biased towards negative, the differences themselves are rather small, less than 0.060 Å. On the other hand, the resolution of our M dwarf spectra is $\text{FWHM} \approx 16 \text{ km s}^{-1}$ or about 1.25 Å. Hence the accuracy of the computed water line list is sufficient for our purpose. We again admire that the computed line positions of water lines can be predicted with such an accuracy.

table 2: p.17

3. ^{13}C features in M dwarfs

The (2,0), (3,1), and (4,2) bands of the first overtone bands of $^{12}\text{C}^{16}\text{O}$ show bandheads at 22935.2, 23226.6, and 23524.6 Å (in vacuum), respectively, and those of $^{13}\text{C}^{16}\text{O}$ at 23448.3, 23739.4, and 24036.9 Å, respectively. The $^{13}\text{C}^{16}\text{O}$ (2,0) and (3,1) bandhead regions are well covered by our observed spectra. However, the (2,0) bandhead region is blended with Ti I line at 23447.87 Å ($a^3\text{G}_4 - z^3\text{F}_3^0$), and this atomic line is pretty disturbing especially in early M dwarfs. The (4,2) bandhead region of $^{13}\text{C}^{16}\text{O}$ is not covered by our observed spectra. Then, we decide to use the (3,1) bandhead region for our analysis of $^{13}\text{C}^{16}\text{O}$.

Predicted spectra of the $^{13}\text{C}^{16}\text{O}$ (3,1) bandhead region (23735 – 23755 Å) for the ^{13}C abundances of 1% and 10% of ^{12}C (or $^{12}\text{C}/^{13}\text{C} = 100$ and 10, respectively) are shown at the top panel of Fig. 1 (Fig. 1a). For this purpose, we apply carbon and oxygen abundances together with model photosphere Ca3570c489 for GJ 15A, as an example (see Table 1). The spectra are first evaluated with a sampling interval of 0.02 Å and then the results are convolved with the slit function (Gaussian) of FWHM = 16 km s⁻¹. The micro-turbulent velocity is assumed to be 1 km s⁻¹ throughout this paper. For comparison, a predicted spectrum of $^{12}\text{C}^{16}\text{O}$ is shown in the second panel of Fig. 1 (Fig. 1b). The bandhead region of $^{13}\text{C}^{16}\text{O}$ is well separated from the strong $^{12}\text{C}^{16}\text{O}$ lines. A predicted spectrum of H₂O in the same region is evaluated with the use of the BT2-HITEMP2010 line-list (Barber et al. 2006; Rothman et al. 2010) and shown in the third panel of Fig. 1 (Fig. 1c).

Composite spectra of $^{13}\text{C}^{16}\text{O}$, $^{12}\text{C}^{16}\text{O}$, and H₂O for $^{12}\text{C}/^{13}\text{C} = 100$ and 10 are shown in the bottom panel of Fig. 1 (Fig. 1d). Features A and F (especially its red wing) are little affected by the $^{13}\text{C}^{16}\text{O}$ lines, and these features are used as references in fitting observed and predicted spectra. On the other hand, features B, C, D, and E show the effect of $^{13}\text{C}^{16}\text{O}$ lines, and can be used to estimate $^{12}\text{C}/^{13}\text{C}$ ratio. Feature B shows the largest isotopic effect due to the contribution of $^{13}\text{C}^{16}\text{O}$ (3,1) bandhead, but this feature is also blended with $^{12}\text{C}^{16}\text{O}$ and H₂O lines (see Figs. 1b and 1c). Feature C is dominated by H₂O lines⁴ except for early M dwarfs (see Fig. 1c), and cannot be a good indicator of isotopic effect. On the other hand, feature D is dominated by the strong R 13 line of $^{13}\text{C}^{16}\text{O}$ (2,0) band at 23745.349 Å, and contributions of $^{12}\text{C}^{16}\text{O}$ and H₂O lines are relatively minor (see Figs. 1b and 1c). For this reason, feature D can be an excellent indicator of $^{13}\text{C}^{16}\text{O}$. Feature E is blended with $^{12}\text{C}^{16}\text{O}$ and H₂O lines, and cannot be useful for our purpose. As for comparison with the observed spectrum of GJ 15A, see Fig. 2b.

Fig. 1: p.10

⁴ The major constituents of feature C are H₂O lines nos. 6, 7, and 8 of Table 2, although about 6000 weak H₂O lines are included in the H₂O spectrum shown in Fig. 1c.

4. Results

4.1. Analysis on carbon isotopic ratios

With our medium resolution spectra, it appears to be rather difficult to determine $^{12}\text{C}/^{13}\text{C}$ by a visual comparison of the observed and predicted spectra. Instead, we apply chi-square (χ^2) analysis to judge goodness of the fits between the observed and predicted spectra. For this purpose, we prepare predicted spectra assuming $^{12}\text{C}/^{13}\text{C} = 10, 25, 50, 100,$ and 200 for the bandhead region of $^{13}\text{C}^{16}\text{O}$ (3,1) band with the physical parameters and abundances summarized in Table 1. The χ_r^2 value for the fitting of the observed spectrum and predicted one for an assumed values of $^{12}\text{C}/^{13}\text{C}$ is evaluated from

$$\chi_r^2(^{12}\text{C}/^{13}\text{C}) = \frac{1}{N-1} \sum_{i=1}^N \left(\frac{f_{\text{obs}}^i - f_{\text{cal}}^i(^{12}\text{C}/^{13}\text{C})}{\sigma_i} \right)^2, \quad (2)$$

where f_{obs}^i and $f_{\text{cal}}^i(^{12}\text{C}/^{13}\text{C})$ are observed and predicted (for a given $^{12}\text{C}/^{13}\text{C}$ value) spectra normalized by their pseudo-continua, respectively, and N is the number of data points. Also, σ_i is the noise level assumed to be constant at 0.01 of the continuum level throughout⁵. Then the resulting χ_r^2 values are on relative scale, which is sufficient for our purpose to find a best $^{12}\text{C}/^{13}\text{C}$ value by the minimization of the χ_r^2 values for each object.

We apply the method outlined above to the observed spectra of 48 M dwarfs listed in Table 3. Some examples are shown Figs. 2a-l, where filled circles are observed spectra and solid lines are predicted ones for $^{12}\text{C}/^{13}\text{C} = 10, 25, 50, 100,$ and 200 (from bottom to top in this order). In Figs. 2a-l, the resulting $^{12}\text{C}/^{13}\text{C}$ value (to be discussed below) is given at the upper left corner of each panel, following the object's name and its spectral type.

We first notice in Figs. 2a-l that feature D in observed spectra of many objects show a concavity, and this should be due to the $^{13}\text{C}^{16}\text{O}$ (2,0) R 13 line at 23745.349 Å, since other contributions such as due to $^{12}\text{C}^{16}\text{O}$ and/or H₂O are not present or very weak in this region as noted in section 3. Thus the concavity in feature D can be regarded as clear evidence for $^{13}\text{C}^{16}\text{O}$, and we are now convinced the presence of a detectable amount of $^{13}\text{C}^{16}\text{O}$ in M dwarfs for the first time. Other ^{13}C indicator such as feature B also shows a concavity but it is not sure if this is due to $^{13}\text{C}^{16}\text{O}$, since this may also be due to $^{12}\text{C}^{16}\text{O}$ and/or H₂O lines as noted in section 3.

We then proceed to the χ^2 analysis to find a best fit between the observed and predicted spectra. The resulting χ_r^2 values for the comparisons of the observed spectrum and predicted spectra for five assumed values of $^{12}\text{C}/^{13}\text{C} = 10, 25, 50, 100,$ and 200 are given through second to sixth column of Table 3 for each of our 48 program stars. Then the minimization of χ_r^2 is done by fitting a parabola that passes through three points near the possible minimum on $\log^{12}\text{C}/^{13}\text{C} - \chi_r^2$ plane for each object.

⁵ The noise levels estimated from the S/N ratios given in the ninth column of Table 3 are about 0.007 – 0.02. We use a median value of 0.01 for all the objects for simplicity, since this value has no effect for the minimization of χ_r^2 values in each object.

Some examples are shown in Fig. 3 for the cases of GJ 876 ($^{12}\text{C}/^{13}\text{C} = 39$), 849 ($^{12}\text{C}/^{13}\text{C} = 67$), 212 ($^{12}\text{C}/^{13}\text{C} = 134$), and 526 ($^{12}\text{C}/^{13}\text{C} > 200$), and the resulting $^{12}\text{C}/^{13}\text{C}$ value corresponding to the minimum of χ_r^2 for each object is given in seventh column of Table 3. Also, the corresponding value of $\log^{13}\text{C}/^{12}\text{C} = -\log^{12}\text{C}/^{13}\text{C}$ is given in eighth column of Table 3 for each object.

From Table 3, we know that some objects show rather low $^{12}\text{C}/^{13}\text{C}$ values (i.e., ^{13}C rich) and values of $^{12}\text{C}/^{13}\text{C}$ are found to be 39, 44, and 49 in GJ 876, 15A, and 179, respectively. These are the most ^{13}C rich cases in our sample, and we could not find more ^{13}C rich cases such as found in some evolved high luminous cool stars. Inspection of Figs. 2a-c reveals that feature D clearly shows the concavity and we are convinced ^{13}C rich nature of these objects. Overall fits such as in features B and C between observed and predicted spectra also appear reasonable for the case of $^{12}\text{C}/^{13}\text{C} \approx 50$ in Figs. 2a-c (remember that the predicted spectra shown by the solid lines are assuming $^{12}\text{C}/^{13}\text{C} = 10, 25, 50, 100, \text{ and } 200$ from bottom to top in each panel).

The χ^2 analysis for GJ 324B suggests $^{12}\text{C}/^{13}\text{C} = 56$, and features B and D are roughly consistent with this result on Fig. 2d. However, feature C appears to suggest $^{12}\text{C}/^{13}\text{C} \approx 25$. But feature C is badly disturbed by H_2O lines and such inconsistency may be fatal for the medium resolution spectra we are using. The χ^2 analysis on GJ 849 suggests $^{12}\text{C}/^{13}\text{C} = 67$, and overall fits are roughly consistent with this result on Fig. 2e. Although the χ^2 analysis for GJ 231.1B suggests $^{12}\text{C}/^{13}\text{C} = 70$ (about the same as for GJ 849), it is more difficult to confirm the overall fits on Fig. 2f. Even though the spectral types of GJ 849 and GJ 231.1B are the same, GJ 849 is hotter by about 100 K and more carbon rich compared with GJ 231.1B (see Table 1). For this reason, H_2O lines are weaker and CO lines are stronger in GJ 849 than in GJ 231.1B, making it easier to investigate isotopic effect on CO spectra in GJ 849.

We find $^{12}\text{C}/^{13}\text{C}$ values to be 80, 90, and 117 in GJ 229, HIP 79431 and GJ 649, respectively, from the χ^2 analysis. Inspection of Figs. 2g-f reveals that feature D in all these three cases clearly shows the concavity and the presence of $^{13}\text{C}^{16}\text{O}$ in these objects are well demonstrated even for the rather large $^{12}\text{C}/^{13}\text{C}$ values (i.e., low ^{13}C abundances). However, to see the overall fits in features B, C, and D are more difficult since the effect of $^{12}\text{C}/^{13}\text{C}$ on the predicted spectra tends to be minor for large $^{12}\text{C}/^{13}\text{C}$ values. We must recognize that it is increasingly difficult to find the best fit by the visual comparison of the observed and predicted spectra and, for this reason, we adopt the χ^2 analysis which is more robust for our purpose.

Such a difficulty in the cases of large $^{12}\text{C}/^{13}\text{C}$ values is more severe in GJ 212 for which the χ^2 analysis suggests $^{12}\text{C}/^{13}\text{C} = 134$, but it is difficult to confirm this result by the visual inspection of Fig. 2j in which predicted spectra for $^{12}\text{C}/^{13}\text{C} = 100$ and 200 differ very little. For GJ 205 shown in Fig. 2k, the χ^2 analysis suggests $^{12}\text{C}/^{13}\text{C} = 140$. Even for such a high value of $^{12}\text{C}/^{13}\text{C}$, feature D clearly shows the concavity and hence presence of $^{13}\text{C}^{16}\text{O}$.

Although this object is classified as dM3, this does not necessarily imply low temperature but this should largely be due to the high metallicity of this object as noted in Paper I. In fact, this object is the most carbon and oxygen rich in our sample (see Table 1). For this reason, CO lines appear to be enhanced and $^{13}\text{C}^{16}\text{O}$ lines as well. Also, H_2O lines, which are disturbing for investigating $^{13}\text{C}^{16}\text{O}$ lines, are not so strong due to higher temperature than that suggested for the spectral type dM3. As a result, this object provides a favorable case for the study of the carbon isotopic ratio. Finally, the χ^2 analysis suggests $^{12}\text{C}/^{13}\text{C} > 200$ for GJ 526 and this result is well consistent with Fig. 2l. For example, feature D does not show the concavity at all, indicating small abundance of $^{13}\text{C}^{16}\text{O}$. More or less similar results of $^{12}\text{C}/^{13}\text{C} > 200$ are obtained for other 16 M dwarfs (e.g., Figs. 4b and 4c).

In principle, it is desirable that the results of the χ^2 analysis could be confirmed to be consistent with the visual comparison of observed and predicted spectra. As we have noticed above, this is difficult especially for the cases of large $^{12}\text{C}/^{13}\text{C}$ values, in which predicted spectra of $^{13}\text{C}^{16}\text{O}$ are already very weak and a difference for the different $^{12}\text{C}/^{13}\text{C}$ values should be still smaller. However, in our χ^2 analysis, we have changed only $^{12}\text{C}/^{13}\text{C}$ values keeping all the other parameters unchanged. Hence the changes of the χ_r^2 values for changed $^{12}\text{C}/^{13}\text{C}$ values should reflect the effect of $^{12}\text{C}/^{13}\text{C}$ alone, and the $^{12}\text{C}/^{13}\text{C}$ value minimizing χ_r^2 should provide the best fit. We must, however, keep in mind that the resolution of our spectra is by no means sufficient for our analysis outlined in this section. For this reason, our result is only very preliminary and we hope that the problem of the carbon isotopic ratios in M dwarfs will be pursued further by higher resolution spectroscopy in the future.

Fig. 2: p.11

Fig. 3: p.12

table 3: p.18

4.2. A binary test

Our sample includes three binary pairs, GJ 338A and 338B, GJ 725A and 725B, and GJ 797B-NE and 797B-SW. Since abundances including isotopic ratios may not be different for the objects in a binary pair⁶, we hope that an assessment of accuracy of our result can be obtained by comparing the results in these binary pairs.

The results of the χ^2 analysis reveal that $^{12}\text{C}/^{13}\text{C} = 105$ and $^{12}\text{C}/^{13}\text{C} > 200$ for GJ 338A and 338B, respectively (see Table 3). Comparisons of the observed and predicted spectra are shown in Figs. 4a and 4b for GJ 338A and 338B, respectively. The results shown in Figs. 4a-b are not much different. But observed and predicted spectra in feature C show some differences in GJ 338A and in

⁶ In fact, the carbon and oxygen abundances in these binary pairs agree within 0.03 dex (note that this is smaller than the probable error of each abundance determination) in all the three cases, as can be confirmed in Table 1.

GJ 338B, and such a difference may be an origin of the different results on $^{12}\text{C}/^{13}\text{C}$ by the χ^2 analysis. However, the predicted spectra for $^{12}\text{C}/^{13}\text{C} = 100$ and 200 are almost indistinguishable in feature C and it should be difficult to decide which of these $^{12}\text{C}/^{13}\text{C}$ values should apply to these M dwarfs. Thus, we must accept uncertainty of about a factor of two in our χ^2 analysis if $^{12}\text{C}/^{13}\text{C} > 100$.

The results of the χ^2 analysis reveal that $^{12}\text{C}/^{13}\text{C} > 200$ and $^{12}\text{C}/^{13}\text{C} = 135$ for GJ 725A and 725B, respectively. Comparisons of the observed and predicted spectra are shown in Figs. 4c and 4d for GJ 725A and 725B, respectively. Again, the results for the two objects are not much different, and to decide which of $^{12}\text{C}/^{13}\text{C} \approx 100$ or 200 should apply to each of these objects appears to be difficult, since the predicted spectra for $^{12}\text{C}/^{13}\text{C} = 100$ and 200 differ little. However, our result of the χ^2 analysis, which is a kind of statistical analysis, suggests $^{12}\text{C}/^{13}\text{C} > 100$ both for GJ 725A and 725B, and we again find consistency within about a factor of two in our analysis.

The results of the χ^2 analysis reveal that $^{12}\text{C}/^{13}\text{C} = 116$ and $^{12}\text{C}/^{13}\text{C} = 93$ for GJ 797B-NE and 797B-SW, respectively. Direct comparisons of the observed and predicted spectra are shown in Figs. 4e and 4f for GJ 797B-NE and 797B-SW, respectively. In this case, the χ^2 method gives the results that agree rather well for this binary pair. Although different features (e.g., B, C, and D) in Fig. 4e and 4f do not necessarily indicate the same $^{12}\text{C}/^{13}\text{C}$ values by visual comparisons, the χ^2 values in Table 3 show the integrated effect of χ^2 values for different features such as B, C, D and E. For this reason, our χ_r^2 values in Table 3 can be a measure of overall fits, and our χ^2 analyses for GJ 797B-NE and 797B-SW show reasonable consistency in the overall fits if not in individual features.

The above results imply that it is difficult to determine $^{12}\text{C}/^{13}\text{C}$ value when it is as large as 200, and if the result of the χ^2 analysis reveals such a result as $^{12}\text{C}/^{13}\text{C} > 200$, it is still possible that actual $^{12}\text{C}/^{13}\text{C}$ may be as low as 100 (e.g., GJ 338B and GJ 725A). Certainly, it is natural that our χ^2 analysis does not work for such small difference which our observed data could not resolve. However, if $^{12}\text{C}/^{13}\text{C} \approx 100$, our binary test suggests that the results agree rather well as in the case of GJ 797B. Although our sample of binary pairs is not large enough, we regard our result of $^{12}\text{C}/^{13}\text{C} > 100$ to be uncertain by about a factor of two but should be better in the case of $^{12}\text{C}/^{13}\text{C} \lesssim 100$.

Fig. 4: p.13

4.3. Further test on the accuracy

Unfortunately, our sample of binary is limited to three pairs and to the cases of rather high $^{12}\text{C}/^{13}\text{C}$ ratios. To extend the similar test to other cases, we use the spectra recorded at A and B positions on slit alternatively during the observation. The resulting spectra are co-added at the end and used for our analysis so far done (Papers I, II, and III; subsections 4.1 and 4.2 in Paper IV). These two

spectra observed at slit positions A and B are recovered separately and we analyze these spectra A and B as if they are independent two spectra. Although S/N ratios of these spectra are reduced by about a factor of $\sqrt{2}$, these spectra can be used in the same way as in the binary test outlined in the previous subsection.

For this purpose, we select M dwarfs of various $^{12}\text{C}/^{13}\text{C}$ ratios and we choose GJ 876, 849, 212, and 526 as examples. These objects cover the $^{12}\text{C}/^{13}\text{C}$ ratios from the smallest to the largest and, for this reason, these objects are already used as representative cases in Fig. 3. The spectra observed at A and B positions are analyzed by essentially the same way as we analyze the co-added spectrum in subsection 4.1 and the results are shown in Figs. 5a-d. The χ_r^2 values for the fitting of the spectrum observed at A or B position and the predicted spectra for five assumed values of the $^{12}\text{C}/^{13}\text{C}$ ratio evaluated by equation (2) are given in second through sixth columns of Table 4. The result of the minimization of χ_r^2 values is given at the last column of Table 4 for each spectrum observed at positions A and B.

The results for the case of GJ 876, which is the most ^{13}C rich in our sample, reveal that the resulting $^{12}\text{C}/^{13}\text{C}$ ratios are 37.7 and 31.4 for the spectra observed at A and B positions (hereafter be referred to as spectra A and B), respectively. Thus, the results for the spectra A and B agree rather well and this may be due to small differences in the features B and D which are most sensitive to the $^{12}\text{C}/^{13}\text{C}$ ratio (Fig. 5a). On the other hand, the resulting $^{12}\text{C}/^{13}\text{C}$ ratios are 59.3 and 108.3 for the spectra A and B, respectively, in the case of GJ 849, and the difference of the $^{12}\text{C}/^{13}\text{C}$ ratios based on the spectra A and B is rather large. This may be due to a considerable difference of the feature D in the observed spectra A and B (Fig. 5b). The S/N ratios for GJ 876 and 849 are not much different (see Table 3), but it appears that the effect of noise on the spectra is rather different and complicated. The resulting $^{12}\text{C}/^{13}\text{C}$ ratios are 106.9 and 139.7 for the spectra A and B, respectively, in the case of GJ 212. The difference of the $^{12}\text{C}/^{13}\text{C}$ ratio based on the spectra A and B is rather modest. In this case, the χ_r^2 values indicates the $^{12}\text{C}/^{13}\text{C}$ ratios not very different, despite some differences in the spectra observed at positions A and B (Fig. 5c). In fact, even if the difference of the observed and predicted spectra (i.e., $f_{\text{obs}}^i - f_{\text{cal}}^i$) at a particular wavelength is disturbed by noise, the χ_r^2 value is determined by including the contributions from other wavelength regions less disturbed by noise as well, and the effect of noise can be averaged in the resulting χ_r^2 value. Finally, the resulting $^{12}\text{C}/^{13}\text{C}$ ratios for the spectra observed at A and B positions for GJ 526 are larger than 200 and 141.0, respectively. Here, the situation is quite similar to the binary pairs GJ 338A,B and GJ 725A,B discussed in subsection 4.2: Since the effect of $^{13}\text{C}^{16}\text{O}$ lines on the spectrum is difficult to discriminate if $^{12}\text{C}/^{13}\text{C} \gtrsim 200$ it is difficult to determine $^{12}\text{C}/^{13}\text{C}$ ratio with the medium resolution we are using.

The results outlined above are summarized in Table 5: For each object, the $^{12}\text{C}/^{13}\text{C}$ ratios based on the spectra observed at A and B positions are shown in second

and third columns, respectively. The mean value of the $^{12}\text{C}/^{13}\text{C}$ ratios based on the spectra at A and B positions is given in fourth column, and the probable error is also estimated. The resulting probable errors appear to be not so large: about 10% in favorable cases (GJ 876, 212) and about 30% in a less favorable case (GJ 849). But uncertainty of as large as a factor of two must be accepted in the poor ^{13}C cases (e.g., GJ 526). The $^{12}\text{C}/^{13}\text{C}$ ratio based on the co-added spectrum is reproduced in fifth column from Table 3. Although an error cannot be estimated from a single spectrum alone, the resulting $^{12}\text{C}/^{13}\text{C}$ ratio is roughly within the error bar estimated in the fourth column by using the spectra with S/N ratios reduced by a factor of $\sqrt{2}$. Thus, we may conclude that the accuracy of our results on the $^{12}\text{C}/^{13}\text{C}$ ratios can be acceptable, and at least better than 50%⁷ except for the cases of the poor ^{13}C (e.g., $^{12}\text{C}/^{13}\text{C} \gtrsim 200$). Although our spectral resolution is not high enough to resolve the individual $^{13}\text{C}^{16}\text{O}$ lines and the S/N ratios are not very high, the χ_r^2 value reflects the integrated effect in the difference of observed and predicted spectra. For this reason, the χ^2 analysis can be a powerful tool for assessment of the goodness of the fitting.

Fig. 5: p.14

table 4: p.19

table 5: p.19

5. Discussion

The unweighted mean value of 48 M dwarfs including those with the lower limit of 200 is $(^{12}\text{C}/^{13}\text{C})_{\text{dM}} > 127 \pm 41$ (p.e.). If we exclude such a case for which only the lower limit of 200 is known, the unweighted mean value of 31 M dwarfs is $(^{12}\text{C}/^{13}\text{C})_{\text{dM}} = 87 \pm 21$ (p.e.). This value agrees well with the value of the solar system, $(^{12}\text{C}/^{13}\text{C})_{\text{SS}} = 89.9$ (Anders & Grevesse 1989). Also, the value of the solar photosphere based on the high resolution infrared solar spectrum is $(^{12}\text{C}/^{13}\text{C})_{\text{Sun}} = 84 \pm 5$ (Harris et al. 1987) or $(^{12}\text{C}/^{13}\text{C})_{\text{Sun}} = 80 \pm 1$ (Ayres et al. 2006). Then the $^{12}\text{C}/^{13}\text{C}$ ratio of the solar photosphere as well as of the solar system is typical of the unevolved late-type dwarfs. However, the scatter of the $^{12}\text{C}/^{13}\text{C}$ ratios in Table 3 is rather large extending from $^{12}\text{C}/^{13}\text{C} = 39$ to $^{12}\text{C}/^{13}\text{C} > 200$ (also see Fig. 6a).

The resulting $^{12}\text{C}/^{13}\text{C}$ values in Table 3 are rewritten as $\log ^{13}\text{C}/^{12}\text{C}$ in eighth column, and plotted against $\log A_{\text{C}}$ in Fig. 6a, where $\log ^{13}\text{C}/^{12}\text{C}$ shows a large scatter without clear dependence on the metallicity. This result shows a marked contrast to the plot of $\log ^{16}\text{O}/^{12}\text{C}$ ($= \log A_{\text{O}}/A_{\text{C}}$ from eighth column of Table 1) against $\log A_{\text{C}}$, which shows a rather tight correlation with a higher ratio at the lower metallicity, as shown in Fig. 6b (reproduced from

Fig. 19 in Paper III). Such a contrast between Figs. 6a and 6b can be a natural consequence that ^{16}O and ^{12}C are the primary products in the stellar nuclear synthesis while ^{13}C is the secondary product, at least partly (e.g., Renzini & Voli 1981). Thus the difference of the primary and secondary products in the actual distribution of the isotopes is clearly demonstrated for the first time.

The $^{12}\text{C}/^{13}\text{C}$ ratios of late-type dwarfs should reflect those of the ISM from which the stars are formed. For comparison, the $^{12}\text{C}/^{13}\text{C}$ ratio in the ISM have extensively been studied by the millimeter spectroscopy of giant molecular clouds. The initial results reviewed by Wannier (1980) show that there is no evidence for a $^{12}\text{C}/^{13}\text{C}$ gradient in the Galactic disk and the mean $^{12}\text{C}/^{13}\text{C}$ ratio is $(^{12}\text{C}/^{13}\text{C})_{\text{ISM}} = 60 \pm 8$, except for the Galactic center source showing $^{12}\text{C}/^{13}\text{C} \approx 20$. However, later results reviewed by Wilson & Rood (1994) clearly indicated an increase of the $^{12}\text{C}/^{13}\text{C}$ ratio with the Galactocentric distance D_{GC} : The $^{12}\text{C}/^{13}\text{C}$ ratio is $(^{12}\text{C}/^{13}\text{C})_{\text{ISM}} \approx 50 \pm 8$ at $D_{\text{GC}} \approx 4$ Kpc and $(^{12}\text{C}/^{13}\text{C})_{\text{ISM}} \approx 76 \pm 7$ at $D_{\text{GC}} \approx 8.5$ Kpc (near the Sun). More recently, the $^{12}\text{C}/^{13}\text{C}$ ratios in the local ISM (within about 1 Kpc of the Sun) have been determined from the optical spectroscopy of $^{13}\text{CH}^+$ absorption lines towards early type stars (Casassus et al. 2005; Stahl et al. 2008) and a significant scatter of $(^{12}\text{C}/^{13}\text{C})_{\text{ISM}} \approx 44 - 147$ was found in the local ISM.

Our result on the $^{12}\text{C}/^{13}\text{C}$ ratios in M dwarfs (Fig. 6a) shows more or less similar pattern to those in the ISM outlined above. For example, the scatter of the $^{12}\text{C}/^{13}\text{C}$ ratio is quite large and extends from ≈ 40 to > 100 both in the ISM and in M dwarfs. Also, such a low ratio as below 40 is not found both in the ISM and in M dwarfs⁸. However, the results on the ISM are on the present ISM at the present locations while our results on M dwarfs may reflect the $^{12}\text{C}/^{13}\text{C}$ ratios of the ISM at various ages when M dwarfs were formed at different birthplaces. For this reason, interpretation of the $^{12}\text{C}/^{13}\text{C}$ ratios in M dwarfs should be more complicated than that in the ISM.

As to the origin of ^{13}C , it is generally thought that ^{13}C is formed from ^{12}C originally present in the star at the time of its formation, and hence ^{13}C is regarded as a typical secondary element. Then, ^{13}C can be produced in almost in all the stars in their hydrogen burning phase and will be dredged-up to the surface by the convective zone developed in the red giant phase (and eventually to ISM by stellar mass loss). However, the temperature at the base of the convective envelope after He shell flash can be high enough for CNO cycle reactions take place (hot bottom burning - HBB), and ^{12}C produced by the He burning can also be converted into ^{13}C . This ^{13}C is primary since it comes from the primary ^{12}C produced from He anew in the star (Renzini & Voli 1981). For this reason, the origin of ^{13}C in the Galaxy is by no means well settled. The chemical evolution of $^{12}\text{C}/^{13}\text{C}$ in the Galaxy has been studied by assuming a mixed origin of primary

⁷ By the way, the $^{12}\text{C}/^{13}\text{C}$ ratio of the binary system GJ 797B can be 104.5 ± 11.0 as a mean of those of its constituents GJ 797B-NE and 797B-SW discussed in subsection 4.2, and again the error of the resulting $^{12}\text{C}/^{13}\text{C}$ ratio can be estimated to be about 10%.

⁸ It was suggested that $^{12}\text{C}/^{13}\text{C} > 15$ for GJ 752B (VB10) by Pavlenko & Jones (2002), using spectra of $\lambda/\Delta\lambda = 1085$ or velocity resolution of 276 km s^{-1} . However, their resolution may be too low to justify their result, as the authors themselves noticed.

and secondary (case A) or a purely secondary origin (case B) (Prantzos et al. 1996). Their results show that the $^{12}\text{C}/^{13}\text{C}$ ratio decreases both in cases A and B during the evolution of the Galaxy, and case A appears to explain somewhat better the present-day $^{12}\text{C}/^{13}\text{C}$ ratio if it is $(^{12}\text{C}/^{13}\text{C})_{\text{ISM}} \approx 70 \pm 10$.

Our result that the mean value of the $^{12}\text{C}/^{13}\text{C}$ ratios in M dwarfs is somewhat larger than that of the present ISM, especially if we consider our result that many M dwarfs show $^{12}\text{C}/^{13}\text{C} > 200$, is well consistent with the decrease of $^{12}\text{C}/^{13}\text{C}$ ratios as a result of chemical evolution of the ISM outlined above. Our result shown in Fig.6 suggests that ^{13}C may be produced as the secondary product, at least partly, and since the secondary process depends on many factors including nuclear reactions, mixing, mass-loss, binarity etc in evolved stars, distribution of $^{12}\text{C}/^{13}\text{C}$ ratios in the ISM and hence in M dwarfs should be inhomogeneous. However, the mean $^{12}\text{C}/^{13}\text{C}$ ratio should decrease with time in the ISM and hence in M dwarfs, resulting in a larger mean $^{12}\text{C}/^{13}\text{C}$ ratio in M dwarfs than that in the present ISM.

The $^{12}\text{C}/^{13}\text{C}$ ratio in M dwarfs in Table 3 and shown in Fig. 6a should reflect the $^{12}\text{C}/^{13}\text{C}$ ratios of the ISM from which M dwarfs were formed, and the $^{12}\text{C}/^{13}\text{C}$ ratio of the ISM itself has been determined by the mass-loss from the stars of the previous generation. It is not possible to know the $^{12}\text{C}/^{13}\text{C}$ ratios of the stars of the previous generation, but we can study the $^{12}\text{C}/^{13}\text{C}$ ratios of similar stars that might have contributed to the $^{12}\text{C}/^{13}\text{C}$ ratios of M dwarf stars. For this purpose, the $^{12}\text{C}/^{13}\text{C}$ ratios in red giants, supergiants, and AGB stars that have been studied by many authors as noted in section 1 can be of some help. For example, if relatively large production of carbon in metal-rich era (Fig. 6b) is due to ABG stars (e.g., Nomoto et al. 2013), the $^{12}\text{C}/^{13}\text{C}$ ratios in unevolved stars as well as in the ISM may be related to those of AGB stars. However, it is not likely that the $^{12}\text{C}/^{13}\text{C}$ ratios observed in the present evolved stars can explain well the $^{12}\text{C}/^{13}\text{C}$ ratio observed in the present ISM as well as in M dwarfs. This should be because the $^{12}\text{C}/^{13}\text{C}$ ratio could be determined only from molecular spectra and the isotopic ratios of many other objects not showing molecular spectra remain unexplored. For this reason, our knowledge on the distribution of isotopes in the Universe is quite limited and imperfect. Unfortunately, this fact makes it difficult to understand observationally the origin of the carbon isotopes in M dwarfs as well as in the ISM.

Other sources of information on the isotopic composition in the Universe are primitive meteorites containing grains of silicon carbide, graphite, diamond etc. Direct analysis on these grains provides accurate isotopic compositions of celestial objects that have produced the grains, and it is no longer limited by the observability of molecular spectra. For example, $^{12}\text{C}/^{13}\text{C}$ ratio obtained from interstellar graphite shows a wide range from near the equilibrium value of the CN cycle to several thousands (e.g., Ott 1993; Amari et al. 1993). Clearly, the dynamic range of the $^{12}\text{C}/^{13}\text{C}$ ratio in meteorite sample is much larger than in ISM and in M dwarfs. We hope that

these results can be incorporated into our understanding on the chemical evolution of isotopes, although it may be by no means easy to identify the origin of each grain.

Fig. 6: p.15

6. Concluding remarks

We have tried to estimate the carbon isotopic ratio $^{12}\text{C}/^{13}\text{C}$ in M dwarfs based on the spectra of medium resolution ($\lambda/\Delta\lambda \approx 20000$). Although this resolution is certainly not sufficient to resolve faint $^{13}\text{C}^{16}\text{O}$ lines from the stronger lines of $^{12}\text{C}^{16}\text{O}$ and H_2O , we find clear evidence for the $^{13}\text{C}^{16}\text{O}$ feature in the spectra of M dwarfs for the first time (see Fig. 1 and Figs. 2a - 1). Then, determination of the $^{12}\text{C}/^{13}\text{C}$ ratios in M dwarfs is quite feasible especially if higher spectral resolution can be employed, and we hope that the isotopic analysis on low luminosity stars such as M dwarfs will be done more intensively as in high luminosity cool stars.

With our medium resolution, we determine a possible best value of $^{12}\text{C}/^{13}\text{C}$ in each M dwarf by comparing observed and predicted spectra, not by a direct inspection but by an application of the chi-square method. Although the direct comparisons (see Figs. 2a - 1, 3a-f) show difficulties inherent to the spectra of insufficient resolution, the chi-square analysis works reasonably well (see Fig. 3). As a result, we determine $^{12}\text{C}/^{13}\text{C}$ ratios for 31 M dwarfs and a lower limit of 200 for 17 M dwarfs. From our preliminary survey, we may suggest that the $^{12}\text{C}/^{13}\text{C}$ ratios in M dwarfs are larger than about 40 and not likely to be so small as in some evolved high luminosity stars. Although the lower limit of the $^{12}\text{C}/^{13}\text{C}$ ratio is found to be 200 in many M dwarfs, this result is uncertain by a factor of two or so. Unfortunately, it is beyond the capability of our medium resolution spectra to analyze faint features due to very low abundance of ^{13}C . We hope that our result can be improved by the use of higher spectral resolutions in the near future.

The mean $^{12}\text{C}/^{13}\text{C}$ ratio in M dwarfs turns out to be larger than that of the ISM (section 5). While the $^{12}\text{C}/^{13}\text{C}$ ratio in the ISM provides the present $^{12}\text{C}/^{13}\text{C}$ ratio, that in M dwarfs reflects the carbon isotopic ratio in the past ISM. So far, the solar system, conserving the $^{12}\text{C}/^{13}\text{C}$ ratio of the ISM 4.5 Gyr ago, was used as a reference in investigating the time variation of the $^{12}\text{C}/^{13}\text{C}$ ratio in the ISM, but M dwarfs can in principle be used for the same purpose with numerous objects in a larger time-space domain. In fact, M dwarfs offer an unique possibility to determine the $^{12}\text{C}/^{13}\text{C}$ ratios in unevolved late-type dwarfs and should have important role to trace the evolution of carbon isotopes (and possibly other isotopes) in the Galaxy. For this reason, determination of isotopic abundances in M dwarfs should be the next major challenge when high resolution infrared spectroscopy will be ripe enough to be able to observe many faint objects not well observed so far.

I thank T. Nakajima for recovering the spectra observed at slit positions A and B before co-adding and for helpful discussion on the evaluation of the S/N ratio. I also thank him and Y. Takeda for sharing the spectra of M dwarfs observed at Subaru IRCS.

I thank the anonymous referee for careful reading of the text and for critical comments especially on the accuracy of the analysis.

This research has made use of the SIMBAD operated at CDS, Strasbourg, France.

Computations are carried out on common use data analysis computing system at the Astronomical Data Center, ADC, of the National Astronomical Observatory of Japan.

References

- Abia, C., & Isern, J. 1997, *MNRAS*, 289, L11
- Allende Prieto, C., Lambert, D. L., & Asplund, M. 2002, *ApJ*, 573, L137
- Amari, S., Hoppe, P., Zinner, E., & Lewis, R. S. 1993, *Nature*, 365, 806
- Anders, E., & Grevesse, N. 1989, *Geochim. Cosmochim. Acta*, 53, 197
- Asplund, M., Grevesse, N., Sauval, A. J., & Scott, P. 2009, *ARA&A*, 47, 481
- Ayres, T. R., Plymate, C., & Keller, C. U. 2006, *ApJS*, 165, 618
- Barber, R. J., Tennyson, J., Harris, G. J., & Tolchenov, R. N. 2006, *MNRAS*, 368, 1087
- Casassus, S., Stahl, O., & Wilson, T. 2005, *A&A*, 441, 181
- Chackerian, C., Jr., & Tipping, R. H. 1983, *J. Mol. Spectros.*, 99, 431
- Day, R. W., Lambert, D. L., & Sneden, C. 1973, *ApJ*, 185, 213
- Dearborn, D. S. P., Eggleton, P. P., & Schramm, D. N. 1976, *ApJ*, 203, 455
- Dearborn, D. S. P., Lambert, D. L., & Tomkin, J. 1975, *ApJ*, 200, 675
- Edvardsson, B., Andersen, J., Gustafsson, B., Lambert, D. L., Nissen, P. E., & Tomkin, J. 1993, *A&A*, 275, 101
- Fujita, Y., & Tsuji, T. 1977, *PASJ*, 29, 711
- Greene, T. F. 1969, *ApJ*, 157, 737
- Guelachivili, G., De Villeneuve, D., Farrenq, R., Urban, W., & Verges, J. 1983, *J. Mol. Spectros.*, 98, 64
- Harris, M. J., Lambert, D. L., & Goldman, A. 1987, *MNRAS*, 224, 237
- Joy, A. H., & Abt, H. A. 1974, *ApJS*, 28, 1
- Kobayashi, N., et al. 2000, *Proc. SPIE*, 4008, 1056
- Lambert, D. L., Dearborn, D. S. P., & Sneden, C. 1974, *ApJ*, 193, 621
- Lambert, D. L., Gustafsson, B., Eriksson, K., & Hinkle, K. H. 1986, *ApJS*, 62, 373
- McKellar, A. 1960, in *Stellar Atmospheres* ed. J. L. Greenstein (Chicago: Univ. Chicago Press), 569
- Menzel, D. H. 1930, *PASP*, 42, 34
- Nomoto, K., Kobayashi, C., & Tominaga, N. 2013, *ARA&A*, 51, 457
- Ohnaka, K., & Tsuji, T. 1996, *A&A*, 310, 933
- Ott, U. 1993, *Nature*, 364, 25
- Pavlenko, Y. V., & Jones, H. R. A. 2002, *A&A*, 396, 967
- Prantzos, N., Aubert, O., & Audouze, J. 1996, *A&A*, 309, 760
- Renzini, A., & Voli, M. 1981, *A&A*, 94, 175
- Rothman, L. S., et al. 2010, *JQSRT*, 111, 2139
- Sanford, R. F. 1929, *PASP*, 41, 271
- Smith, V. V., & Lambert, D. L. 1986, *ApJ*, 311, 843
- Smith, V. V., & Lambert, D. L. 1990, *ApJS*, 72, 387
- Stahl, O., Casassus, S., & Wilson, T. 2008, *A&A*, 477, 865
- Tomkin, J., & Lambert, D. L. 1974, *ApJ*, 193, 631
- Tomkin, J., Lambert, D. L., & Luck, R. E. 1975, *ApJ*, 199, 436
- Tsuji, T. 2002, *ApJ*, 575, 264
- Tsuji, T. 2008, *A&A*, 489, 1271
- Tsuji, T., & Nakajima, T. 2014, *PASJ*, 66, 98 (Paper I)
- Tsuji, T., & Nakajima, T. 2016, *PASJ*, 68, 13 (Paper III)
- Tsuji, T., Nakajima, T., & Takeda, Y. 2015, *PASJ*, 67, 26 (Paper II)
- Wallace, L., & Livingston, W. 1992, N. S. O. Technical Report No.92-001, *An Atlas of a Dark Sunspot Umbral Spectrum in the Infrared from 1970 to 8640 cm⁻¹* (Tucson: NOAO)
- Wannier, P. G. 1980, *ARA&A*, 18, 399
- Wilson, T. L., & Rood, R. T. 1994, *ARA&A*, 32, 191

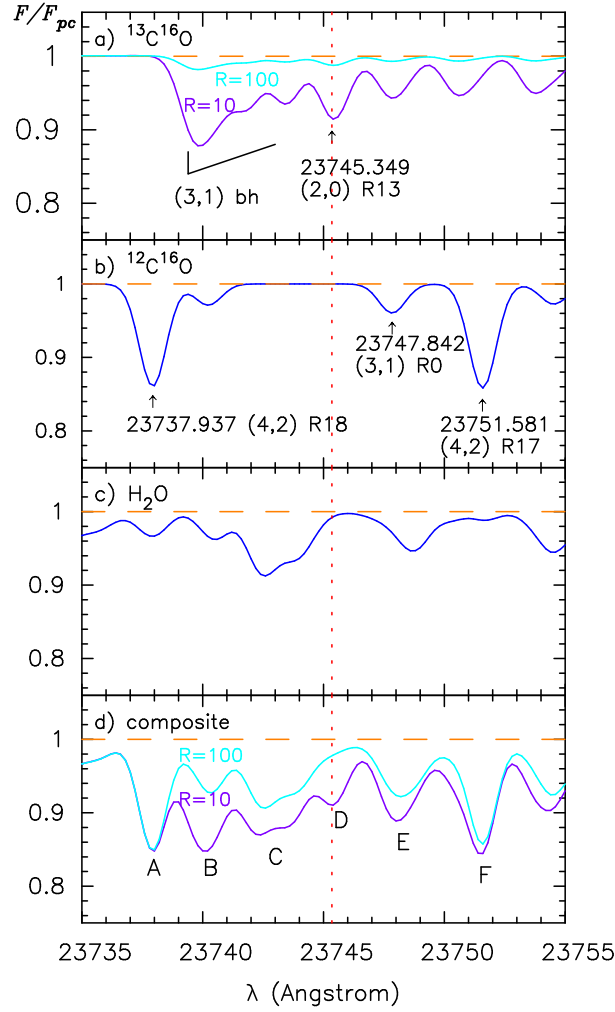


Fig. 1. Model spectra near the bandhead region of $^{13}\text{C}^{16}\text{O}$ (3,1) band based on $\log A_{\text{C}} = -3.60$, $\log A_{\text{O}} = -3.31$, and Ca3570c489: a) for $^{13}\text{C}^{16}\text{O}$ alone, assuming $^{12}\text{C}/^{13}\text{C} = R = 10$ and 100 . b) for $^{12}\text{C}^{16}\text{O}$ alone. c) for H_2O alone. d) for composite of $^{13}\text{C}^{16}\text{O}$ (assuming $^{12}\text{C}/^{13}\text{C} = R = 10$ and 100), $^{12}\text{C}^{16}\text{O}$, and H_2O . Features A and E (red wing) are mostly due to $^{12}\text{C}^{16}\text{O}$. Feature B is dominated by $^{13}\text{C}^{16}\text{O}$ (3,1) bandhead but disturbed by $^{12}\text{C}^{16}\text{O}$ and H_2O lines. Feature C is dominated by H_2O lines except for early M dwarfs. Feature D is dominated by $^{13}\text{C}^{16}\text{O}$ (2,0) R13 line without serious blending with $^{12}\text{C}^{16}\text{O}$ and H_2O lines, and can be an excellent indicator of $^{13}\text{C}^{16}\text{O}$.

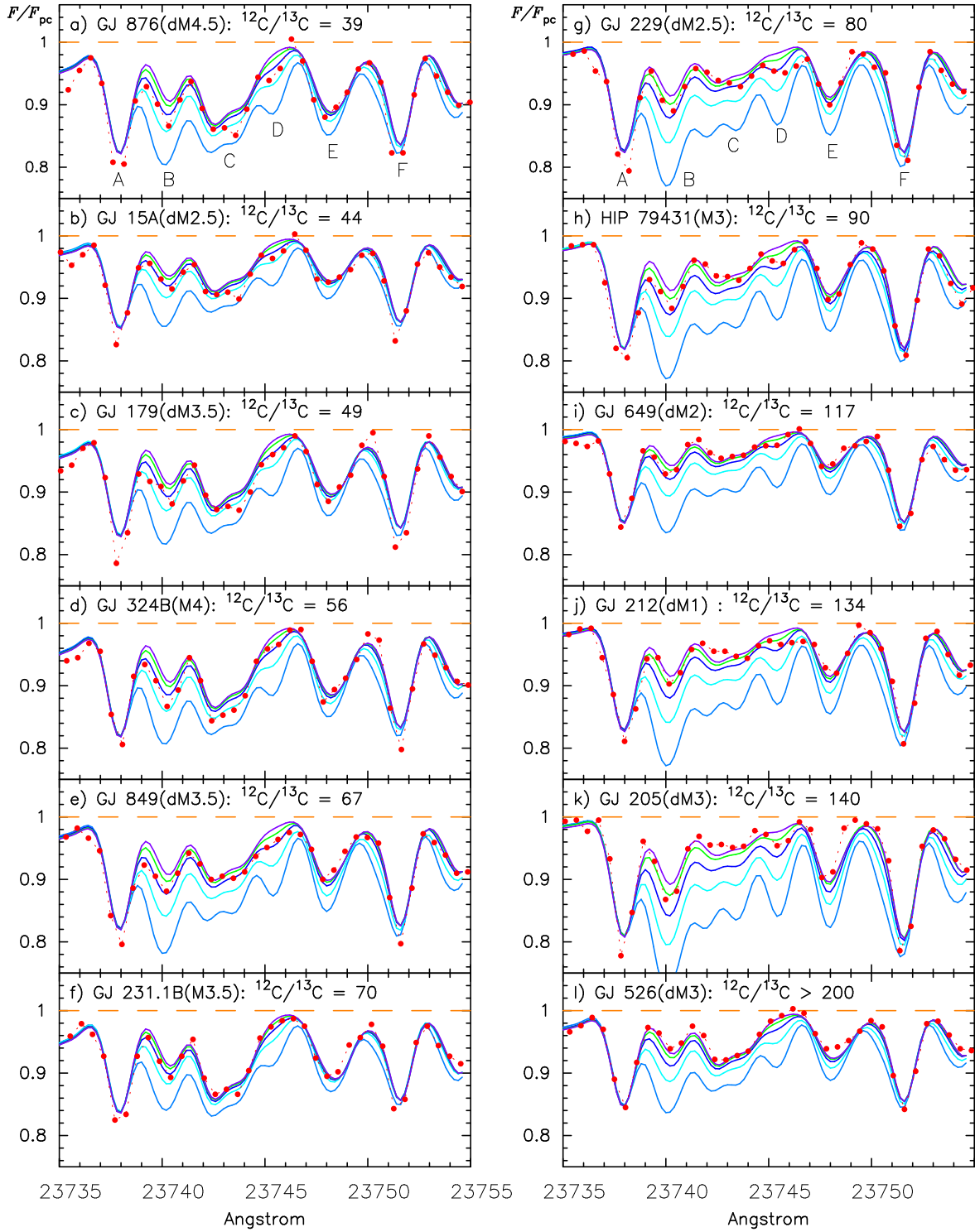


Fig. 2. Comparisons of the observed spectrum (filled circles) and predicted spectra for $^{12}\text{C}/^{13}\text{C} = 10, 25, 50, 100,$ and 200 (solid lines from bottom to top in this order) in each panel. The object identification, spectral type, and resulting $^{12}\text{C}/^{13}\text{C}$ value are indicated at the upper left corner for each object.

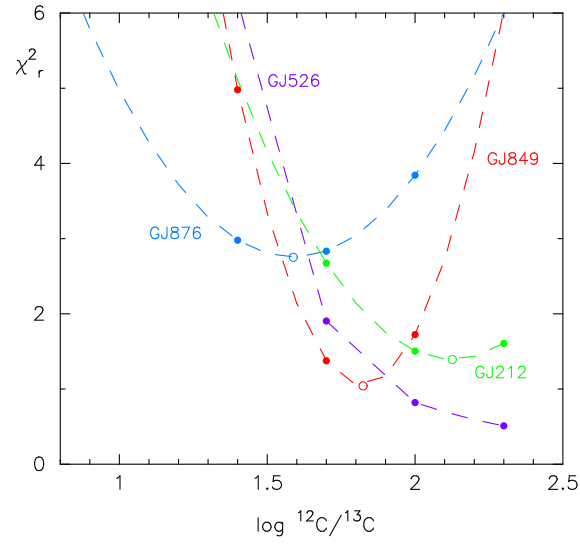


Fig. 3. The χ_r^2 values given in Table 3 are plotted against $\log ^{12}\text{C}/^{13}\text{C}$ for GJ 876, 849, 212, and 526, as examples. A parabola is fitted to three data points (filled circles) near the possible minimum and minimized χ_r^2 value is shown by an open circle for each object. However, the χ_r^2 value for GJ 526 shows no minimum and continues to decrease until $^{12}\text{C}/^{13}\text{C} = 200$. Then, we can determine only the lower limit of $^{12}\text{C}/^{13}\text{C}$ to be 200.

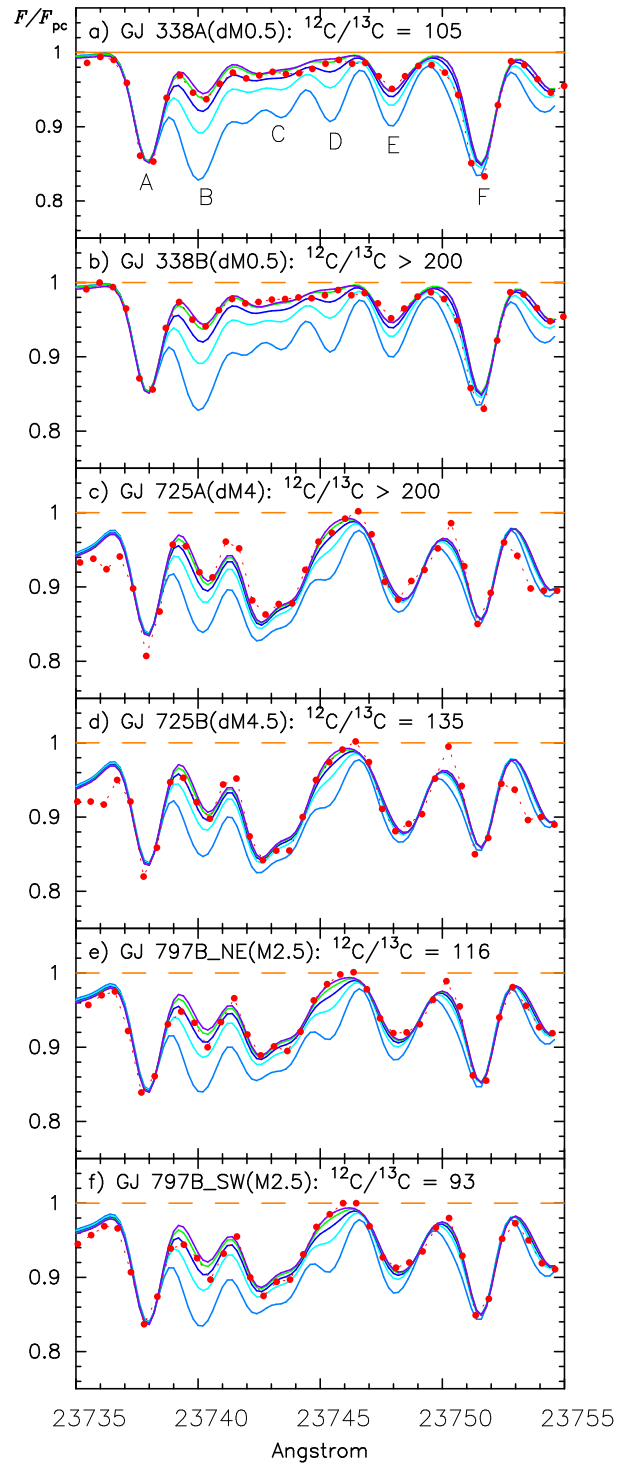


Fig. 4. The same as in Fig. 2, but compare the results for binary pairs: a) GJ 338A and b) GJ 338B, c) GJ 725A and d) GJ 725B, and e) GJ 797B-NE and f) GJ 797B-SW. Other details in each panel are the same as in Fig. 2.

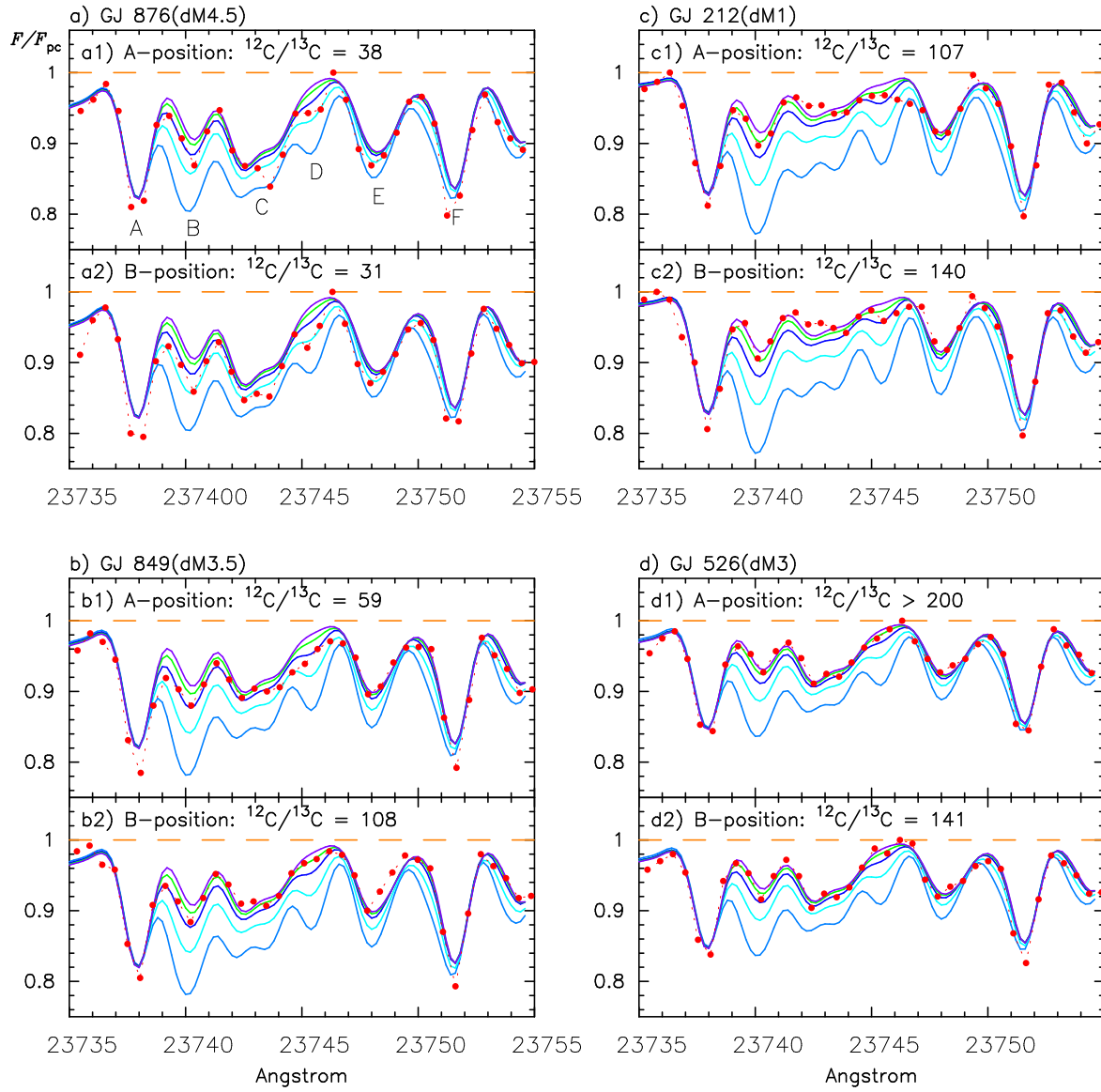


Fig. 5. The same as in Fig. 4, but compare the results for the spectra observed at positions A and B on the slit: a) GJ 876, b) GJ 849, c) GJ 212, and d) GJ 526. In each object, upper panel shows the result for the spectrum observed at position A and the lower panel at position B.

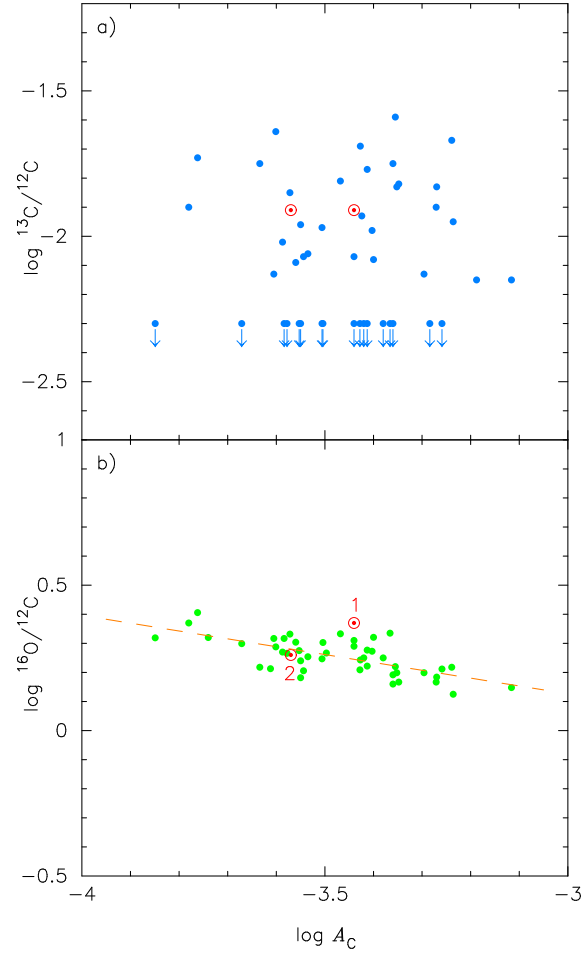


Fig. 6. a) The values of $\log^{13}\text{C}/^{12}\text{C}$ from Table 3 are plotted against $\log A_C$. Arrows indicate upper limits. The case of the solar photosphere marked by \odot is a mean value by Harris et al. (1987) and by Ayres et al. (2006). b) The values of $\log^{16}\text{O}/^{12}\text{C}$ ($= \log A_O/A_C$ from Table 1) are plotted against $\log A_C$. The dashed line is a least square fit to the 46 data (equation 1 in subsection 2.2) excluding the solar data. Two cases for the solar photosphere by Anders & Grevesse (1989) and by Asplund et al. (2009) are shown by \odot attached 1 and 2, respectively.

Table 1. Fundamental parameters, model photospheres, and C & O abundances for 50 M dwarfs.

obj.	Sp. Type*	T_{eff}^{\dagger}	$\log g^{\dagger}$	model [‡]	$\log A_{\text{C}} \pm \text{p.e.}^{\dagger}$	$\log A_{\text{O}} \pm \text{p.e.}^{\S}$	$\log A_{\text{O}}/A_{\text{C}}$
GJ 15A	dM2.5	3567	4.890	Ca3570c489	-3.60 ± 0.11	-3.31 ± 0.01	0.29
GJ 54.1	dM5.5e	3162	5.083	Ca3160c508	-3.38 ± 0.09	-3.13 ± 0.06	0.25
GJ 105B	dM4.5	3360	4.954	Ca3360c495	-3.47 ± 0.06	-3.14 ± 0.04	0.33
GJ 166C	dM4e	3337	4.972	Ca3340c497	-3.37 ± 0.14	-3.03 ± 0.06	0.34
GJ 176	dM2.5e	3616	4.804	Ca3620c480	-3.35 ± 0.07	-3.15 ± 0.02	0.20
GJ 179	dM3.5e	3476	4.877	Ca3480c488	-3.43 ± 0.11	-3.18 ± 0.04	0.24
GJ 205	dM3	3801	4.710	Ca3800c471	-3.12 ± 0.08	-2.97 ± 0.05	0.15
GJ 212	dM1	3757	4.748	Ca3760c475	-3.30 ± 0.11	-3.10 ± 0.03	0.20
GJ 229	dM2.5	3707	4.766	Ca3710c477	-3.27 ± 0.07	-3.10 ± 0.02	0.17
GJ 231.1B	M3.5	3442	4.897	Ca3440c490	-3.57 ± 0.05	-3.24 ± 0.05	0.33
GJ 250B	M2	3567	4.827	Ca3570c483	-3.41 ± 0.10	-3.19 ± 0.03	0.22
GJ 273	dM4	3415	4.915	Ca3420c492	-3.40 ± 0.11	-3.13 ± 0.04	0.27
GJ 324B	M4	3382	4.938	Ca3380c494	-3.36 ± 0.13	-3.17 ± 0.04	0.19
GJ 338A	dM0.5	3907	4.709	Ca3910c471	-3.59 ± 0.04	-3.32 ± 0.03	0.27
GJ 338B	dM0.5	3867	4.709	Ca3870c471	-3.58 ± 0.04	-3.31 ± 0.06	0.27
GJ 380	dM0.5	4081	4.643	Ca4080c464	-3.28 ± 0.06	-3.08	0.20
GJ 406	dM6.5e	2800	5.170	Cc2800c517	-3.61 ± 0.10	-3.40 ± 0.03	0.21
GJ 411	dM2	3465	4.857	Cc3470c486	-3.67 ± 0.06	-3.37 ± 0.03	0.30
GJ 412A	dM2	3497	4.843	Cc3500c484	-3.85 ± 0.04	-3.53 ± 0.03	0.32
GJ 436	dM3.5	3416	4.797	Cc3420c480	-3.63 ± 0.06	-3.42 ± 0.02	0.22
GJ 526	dM3	3618	4.784	Cc3620c478	-3.55 ± 0.04	-3.28 ± 0.03	0.27
GJ 581	dM4	3442	4.959	Ca3440c496	-3.56 ± 0.05	-3.26 ± 0.03	0.30
GJ 611B	M4	3202	5.063	Cc3200c506	-3.76 ± 0.03	-3.36 ± 0.06	0.41
GJ 649	dM2	3660	4.784	Ca3660c478	-3.54 ± 0.04	-3.34 ± 0.03	0.21
GJ 686	dM1	3538	4.842	Ca3540c484	-3.50 ± 0.04	-3.23 ± 0.03	0.27
GJ 687	dM4	3413	4.811	Ca3410c481	-3.43 ± 0.09	-3.22 ± 0.03	0.21
GJ 725A	dM4	3407	4.837	Cc3410c484	-3.58 ± 0.09	-3.27 ± 0.05	0.32
GJ 725B	dM4.5	3337	4.972	Cc3340c497	-3.61 ± 0.08	-3.29 ± 0.06	0.32
GJ 752B	M8	2637	5.213	Cc2640c521	-3.55 ± 0.07	-3.31 ± 0.04	0.24
GJ 768.1C		3470	4.881	Ca3470c488	-3.50 ± 0.08	-3.20 ± 0.04	0.30
GJ 777B	M4.5	3310	4.991	Ca3310c499	-3.24 ± 0.16	-3.02 ± 0.05	0.22
GJ 783.2B	M4	3370	4.949	Ca3370c495	-3.41 ± 0.10	-3.14 ± 0.05	0.28
GJ 797B-NE	M2.5	3473	4.878	Ca3470c488	-3.54 ± 0.09	-3.28 ± 0.03	0.25
GJ 797B-SW	M2.5	3473	4.878	Ca3470c488	-3.51 ± 0.09	-3.26 ± 0.03	0.25
GJ 809	dM2	3692	4.720	Ca3690c472	-3.55 ± 0.04	-3.37 ± 0.03	0.18
GJ 820B	dM0	3932	4.679	Ca3930c468	-3.51 ± 0.05	-3.25	0.26
GJ 849	dM3.5	3580	4.821	Ca3580c482	-3.27 ± 0.09	-3.09 ± 0.02	0.18
GJ 873	dM4.5e	3434	4.903	Ca3430c490	-3.44 ± 0.09	-3.13 ± 0.06	0.31
GJ 876	dM4.5	3458	4.888	Ca3460c489	-3.36 ± 0.13	-3.14 ± 0.04	0.22
GJ 880	dM2.5	3713	4.716	Ca3710c472	-3.35 ± 0.07	-3.18 ± 0.03	0.17
GJ 884	dM0.5	3850	4.720	Ca3850c472	-3.42 ± 0.07	-3.18	0.24
GJ 1002	M5.5	2974	5.123	Ca2970c513	-3.42 ± 0.09	-3.17 ± 0.05	0.25
GJ 1245B	M5.5	2944	5.138	Ca2940c514	-3.44 ± 0.10	-3.15 ± 0.07	0.29
GJ 3348B	M4	3476	4.876	Ca3480c488	-3.40 ± 0.11	-3.08 ± 0.05	0.32
HIP 12961	M0	3890	4.709	Ca3890c471	-3.19 ± 0.07	-3.01	0.18
HIP 57050	M4	3464	4.884	Ca3460c488	-3.26 ± 0.12	-3.05 ± 0.04	0.21
HIP 79431	M3	3592	4.815	Ca3590c482	-3.24 ± 0.12	-3.11 ± 0.01	0.12
GAT 1370	M8/9	2685	5.199	Cc2690c520	-3.78 ± 0.06	-3.41 ± 0.06	0.37
LP 412-31	M8	2607	5.217	Ca2610c522	-3.36 ± 0.07	-3.20 ± 0.03	0.16
2MASS 1835+32	M8.5	2275	5.261	Bc2280c526	-3.74 ± 0.13	-3.42 ± 0.02	0.32
the Sun 1					-3.44 ± 0.04	-3.07 ± 0.035	0.37
the Sun 2 [#]					-3.57 ± 0.05	-3.31 ± 0.05	0.26

* Spectral types beginning with dM are from Joy & Abt (1974) and those beginning with M from SIMBAD.

† from Paper I or III.

‡ Specified model for T_{eff} and $\log g$ in columns 3 and 4, respectively, from Paper I or III.§ from Paper II or III. Those without p.e. are estimated from $\log A_{\text{C}}$ based on $\log A_{\text{O}}/A_{\text{C}}$ by equation 1.

|| Anders & Grevesse (1989).

Asplund et al. (2009).

Table 2. Comparison of the observed and computed line positions of H₂O.

no.	$\nu_{\text{obs}}(\text{cm}^{-1})$ *	$\nu_{\text{cal}}(\text{cm}^{-1})$ †	$\lambda_{\text{obs}}(\text{\AA})$ ‡	$\lambda_{\text{cal}}(\text{\AA})$ ‡	diff.	$v'_1 v'_2 v'_3$	$v''_1 v''_2 v''_3$	J'	K'_a	K'_c	J''	K''_a	K''_c
1	4203.8462	4203.8450	23787.740	23787.747	-0.007	100	000	17	12	5	16	11	6
2	4204.2840	4204.2750	23785.263	23785.314	-0.051	100	000	17	16	1	16	15	2
3	4205.4124	4205.4110	23778.881	23778.889	-0.008	100	000	17	9	9	16	8	8
4	4206.7835	4206.7830	23771.131	23771.133	-0.003	100	000	17	9	8	16	8	9
5	4208.4149	4208.4120	23761.916	23761.932	-0.016	100	000	17	14	3	16	13	4
6	4211.5887	4211.5830	23744.009	23744.041	-0.032	100	000	19	10	9	18	9	10
7	4211.7144	4211.7110	23743.300	23743.320	-0.019	100	000	18	18	1	17	17	0
8	4211.8684	4211.8610	23742.432	23742.474	-0.042	100	000	18	11	8	17	10	7
9	4214.3640	4214.3610	23728.373	23728.390	-0.017	100	000	15	5	10	14	4	11
10	4220.0551	4220.0530	23696.373	23696.385	-0.012	100	000	18	9	10	17	8	9
11	4220.5941	4220.5860	23693.347	23693.392	-0.045	100	000	18	16	3	17	15	2
12	4226.5447	4226.5450	23659.989	23659.987	+0.002	100	000	19	18	1	18	17	2
13	4234.2558	4234.2450	23616.901	23616.961	-0.060	100	000	19	12	7	18	11	8
14	4238.7311	4238.7270	23591.966	23591.989	-0.023	100	000	19	15	4	18	14	5

* measured from the digital version of the Sunspot Umbral Spectrum (Wallace & Livingston 1992).

† from BT2-HITEMP2010 (Barber et al. 2006; Rothman et al. 2010).

‡ in vacuum.

Table 3. $\chi_r^2(^{12}\text{C}/^{13}\text{C})$ for five values of $^{12}\text{C}/^{13}\text{C}$, $^{12}\text{C}/^{13}\text{C}$ for the χ_r^2 minimum, $\log^{13}\text{C}/^{12}\text{C}$ and S/N ratio.

obj.	$\chi_r^2(10)$	$\chi_r^2(25)$	$\chi_r^2(50)$	$\chi_r^2(100)$	$\chi_r^2(200)$	$^{12}\text{C}/^{13}\text{C}(\chi_{\min}^2)^*$	$\log^{13}\text{C}/^{12}\text{C}$	S/N
GJ 15A	7.913	1.851	1.648	2.108	2.515	44	-1.64	78
GJ 54.1	22.076	7.466	4.739	3.918	3.698	>200	< -2.30	45
GJ 105B	9.951	4.088	3.416	3.536	3.775	64	-1.81	70
GJ 166C	18.002	7.224	5.155	4.512	4.345	>200	< -2.30	63
GJ 176	23.169	4.497	1.891	2.078	2.744	68	-1.83	71
GJ 179	13.845	3.605	3.072	3.705	4.361	49	-1.69	68
GJ 205	67.790	21.498	7.137	3.194	3.241	140	-2.15	64
GJ 212	41.244	10.138	2.674	1.505	1.607	134	-2.13	63
GJ 229	35.496	7.866	2.706	2.525	3.363	80	-1.90	64
GJ 231.1B	10.690	2.546	1.638	1.644	1.808	70	-1.85	126
GJ 250B	28.015	9.063	3.434	2.327	2.153	>200	< -2.30	72
GJ 273	15.595	4.217	2.657	2.517	2.701	95	-1.98	69
GJ 324B	15.074	3.276	2.168	2.730	3.400	56	-1.75	120
GJ 338A	21.385	3.691	0.964	0.922	0.954	105	-2.02	114
GJ 338B	24.078	4.740	1.249	0.751	0.690	>200	< -2.30	120
GJ 380	76.979	24.081	8.305	3.181	1.908	>200	< -2.30	59
GJ 406	25.263	6.778	3.754	3.600	3.850	92	-1.96	55
GJ 411	11.006	2.372	1.123	0.875	0.874	>200	< -2.30	119
GJ 412A	8.083	3.692	3.053	2.910	2.894	>200	< -2.30	135
GJ 436	9.841	2.158	1.537	1.852	2.215	56	-1.95	109
GJ 526	21.705	6.160	1.905	0.820	0.510	>200	< -2.30	118
GJ 581	12.142	3.158	1.878	1.672	1.721	124	-2.09	105
GJ 611B	5.685	3.593	3.427	3.534	3.649	54	-1.73	95
GJ 649	20.342	3.983	1.386	1.069	1.188	117	-2.07	114
GJ 687	28.257	8.680	3.838	2.771	2.570	>200	< -2.30	124
GJ 725A	14.798	5.524	3.693	3.163	3.041	>200	< -2.30	165
GJ 725B	10.967	4.702	3.657	3.453	3.467	135	-2.13	91
GJ 752B	38.982	13.280	7.916	6.825	6.408	>200	< -2.30	64
GJ 768.1C	21.125	5.977	3.398	2.672	2.493	>200	< -2.30	86
GJ 777B	14.325	6.440	6.015	6.619	7.302	47	-1.67	73
GJ 783.2B	11.072	3.796	3.128	3.355	3.705	59	-1.77	152
GJ 797B-NE	13.402	2.828	1.129	0.892	0.989	116	-2.06	130
GJ 797B-SW	12.733	2.467	0.936	0.821	0.998	93	-1.97	130
GJ 809	23.483	4.948	1.809	1.659	1.898	92	-1.96	94
GJ 820B	38.247	9.876	3.407	1.700	1.375	>200	< -2.30	77
GJ 849	23.646	4.981	1.376	1.725	2.617	67	-1.83	72
GJ 873	15.949	4.170	2.456	2.197	2.292	117	-2.07	46
GJ 876	13.128	2.979	2.833	3.843	4.775	39	-1.59	71
GJ 880	30.162	5.856	2.273	2.655	3.593	66	-1.82	70
GJ 884	29.031	6.078	2.398	2.229	2.686	85	-1.93	62
GJ 1002	22.928	6.077	3.299	2.642	2.560	>200	< -2.30	76
GJ 1245B	24.179	8.541	6.013	5.440	5.366	>200	< -2.30	45
GJ 3348B	16.424	3.878	1.980	1.676	1.775	119	-2.08	99
HIP 12961	60.679	17.211	4.949	2.044	2.092	140	-2.15	59
HIP 57050	34.777	10.965	4.118	2.202	1.625	>200	< -2.30	140
HIP 79431	34.252	7.670	2.597	2.195	2.957	90	-1.95	93
GAT 1370	14.485	9.067	8.327	8.178	8.938	79	-1.90	69
LP 412-31	71.340	23.198	9.200	4.081	3.780	>200	< -2.30	58
the Sun [†]						82	-1.91	

* $^{12}\text{C}/^{13}\text{C}$ at which χ_r^2 is minimum.† $(^{12}\text{C}/^{13}\text{C})_{\text{Sun}}$ is the mean value of the solar photosphere by Harris et al. (1987) and by Ayres et al. (2006).

Table 4. $\chi_r^2(^{12}\text{C}/^{13}\text{C})$ for five values of $^{12}\text{C}/^{13}\text{C}$, and $^{12}\text{C}/^{13}\text{C}$ for the χ_r^2 minimum.

obj.*	$\chi_r^2(10)$	$\chi_r^2(25)$	$\chi_r^2(50)$	$\chi_r^2(100)$	$\chi_r^2(200)$	$^{12}\text{C}/^{13}\text{C}(\chi_{\min}^2)^\dagger$
GJ 876-A	14.009	3.840	3.746	4.726	5.638	37.7
GJ 876-B	11.143	3.385	4.437	5.962	7.173	31.4
GJ 849-A	21.499	4.654	2.335	3.140	4.282	59.3
GJ 849-B	30.090	8.070	2.104	1.516	1.883	108.3
GJ 212-A	36.859	8.519	2.591	1.915	2.371	106.9
GJ 212-B	42.102	11.035	3.537	2.211	2.232	139.7
GJ 526-A	18.447	4.640	1.514	0.901	0.836	>200.0
GJ 526-B	17.125	4.459	1.812	1.351	1.352	141.0

* A and B after object name refer to the positons A and B on the slit and should not be confused with the binary componets.

† $^{12}\text{C}/^{13}\text{C}$ at which χ_r^2 is minimum.

Table 5. $^{12}\text{C}/^{13}\text{C}$ ratios based on separated A, B, and co-added spectra.

obj.	$(^{12}\text{C}/^{13}\text{C})_A^*$	$(^{12}\text{C}/^{13}\text{C})_B^\dagger$	$(^{12}\text{C}/^{13}\text{C})_{\text{mean}} \pm \text{p.e.}^\ddagger$	$(^{12}\text{C}/^{13}\text{C})_{A+B}^\S$
GJ876	37.7	31.4	34.6 ± 3.0	39
GJ849	59.3	108.3	83.8 ± 23.4	67
GJ212	106.9	139.7	123.3 ± 15.6	134
GJ526	>200.0	141.0		>200

* based on the spectrum at position A (from Table 4).

† based on the spectrum at position B (from Table 4).

‡ mean of the results based on the spectra at positions A and B.

§ based on the coadded spectrum (from Table 3).